UNIVERSITY OF CALIFORNIA

Los Angeles

High-Resolution Multi-View Light-Sheet Imaging System with Comprehensive Tissue Clearing Compatibility and Large Field of View

A thesis submitted in partial satisfaction

of the requirements for the degree

Master of Science in Bioengineering

by

Yaran Zhang

2024

ABSTRACT OF THE THESIS

High-Resolution Multi-View Light-Sheet Imaging System with Comprehensive Tissue Clearing Compatibility and Large Field of View

by

Yaran Zhang

Master of Science in Bioengineering

University of California, Los Angeles, 2024

Professor Tzung Hsiai, Chair

Light-sheet fluorescence microscopy stands out in the field of bioimaging as its rapid imaging speed, deep penetration depth, and reduced phototoxicity and photobleaching. However, an essential step in imaging large tissues is optical clearing. This process removes lipids, pigments, and calcium phosphate, which are not conducive to clear imaging, and matches the specimen's refractive index with the imaging medium to achieve high transparency. Numerous optical clearing strategies are employed, categorized into three main types: hydrophobic, hydrophilic, and hydrogel-based, each with distinct refractive indices. Typically, biologists design an optical system tailored to a specific sample and clearing method, restricting it to one fixed refractive index.

This thesis hereby proposes a light-sheet system compatible with various tissue clearing methods with large field of view. The system also integrates multi-view reconstruction algorithm to maintain stable high resolution. Its performance is assessed by measuring the point spread function and imaging different specimens: *Tg(flk1:mcherry)* zebrafish in water, mouse retina cleared by CLARITY, $\alpha\mathrm{MHC}^{\mathrm{Cre}}$; $\mathrm{R26}^{\mathrm{VT2/GK}}$ mouse rainbow heart cleared by CUBIC, and mouse descending aorta cleared by iDISCO+. The system demonstrated robustness across multiple optical clearing approaches while maintaining high resolution and a large field of view. It offers the possibility for biologists to explore diverse tissue clearing strategies and study various tissues using a single system.

The thesis of Yaran Zhang is approved.

Jennifer Lynn Wilson

Liang Gao

Tzung Hsiai, Committee Chair

University of California, Los Angeles

2024

Table of Contents

LIST OF FIGURES

ACKNOWLEDGEMENTS

I extend my sincere gratitude to all my committee members, Prof. Tzung Hsiai, Dr. Liang Gao, and Dr. Jennifer Wilson, for their invaluable suggestions on this project. I am especially grateful to Prof. Tzung Hsiai for providing me with opportunities to work in his remarkable lab. His mentorship has been instrumental in shaping my understanding and completion of this work, as well as in guiding me towards my future goals.

I am grateful to Dr. Enbo Zhu for his mentorship throughout this project. His experience as a post-doc provided invaluable guidance and insightful suggestions, which greatly contributed to our collaborative efforts. Each chapter of this work reflects both our joint endeavors and my individual contributions. This work is now in preparation for submission.

I would also like to thank all the members of the Hsiai lab for their patience and support throughout my journey here. Working alongside them has been a great pleasure, and their assistance has been invaluable to me.

Lastly, I am immensely thankful to my mother, my family, and my friends, with special mention to Z.W, T.L, W.Z, and V.J, for their unwavering companionship and support. I also want to thank my dog, Luca, whose boundless love and comforting presence have been a source of constant joy and encouragement. Without them, I would not have reached this point.

CHAPTER 1 Introduction

1.1 Optical Imaging in Biology

Wide-field microscopy, which evolved from bright-field microscopy and integrates fluorescence to offer significantly detailed insights into cellular processes, represents a landmark achievement in the history of optical imaging for biologists. Since then, optical microscopy has been pivotal in enhancing our understanding of the biological realm since its inception [1]. In wide-field microscopy, the entire specimen is illuminated simultaneously, resulting in a significant amount of unfocused background signal. This out-of-focus light reduces the microscope's ability to produce high-contrast and high-resolution images. To address this issue, extensive efforts have been made to develop more advanced techniques. Innovations such as confocal microscopy and two-photon microscopy have allowed researchers to observe and quantify biological structures with remarkable detail [2–4].

Laser scanning confocal microscopy (LSCM) came forth as a powerful tool for biological imaging by using a pinhole in front of the detector to reject out-of-focus light. This enhancement significantly improves both contrast and resolution, allowing for the detailed revelation of complex morphologies [5]. Given the limited imaging speed of LSCM, spinning disk confocal microscopy (SDCM) was developed. It features a rapidly rotating disk with numerous pinholes, allowing simultaneous scanning of these focal points. This design achieves faster imaging speed and enables live-cell imaging [6].

Two-photon laser scanning microscopy (2PLSM) is another competitive tool used in biological imaging field. Unlike conventional microscopy methods, 2PLSM employs the simultaneous absorption of two photons to excite fluorophores within the specimen. This enables deeper light penetration in the tissue, making it a great option for large and thick samples. Additionally, by using longer excitation wavelengths, 2PLSM reduces the potential for phototoxicity, allowing for prolonged imaging sessions without damaging the specimen [7,8].

Despite all the above imaging techniques advancements, they are not without limitations. Challenges including prolonged data acquisition times, phototoxicity and photobleaching, and limited penetration depth can hamper their effectiveness in certain applications, thus, prompting the exploration of alternative microscopy methods [2,9–12].A significant breakthrough occurred with the introduction of light-sheet fluorescence microscopy (LSFM) [13], which offers rapid imaging speeds and deeper imaging capabilities, and is suitable for both two-dimensional (2D) and three-dimensional (3D) bioimaging [14,15].

LSFM, as the name indicates, employes a thin ‘sheet‘ of light to illuminate only a slice of the sample. Because it captures data solely from this plane, the laser intensity required can be reduced. In typical light-sheet systems, the excitation beam is placed in orthogonal to the detection camera to collect fluorescence signals. This design markedly diminishes out-of-focus light, inherently providing high-resolution 3D optical sectioning while simultaneously minimizing photobleaching [16,17]. It also enables LSFM to acquire more than double the imaging depth of LSCM [18], making it an invaluable tool in biological research [19–21]. Applications of LSFM include imaging of subcellular, inter- or intracellular processes, and even the long-term development of model systems.

While LSFM excels in three-dimensional imaging, it faces several limitations. One such constraint is the anisotropy and relatively low vertical resolution [22–24]. However, the application of multi-view algorithms can mitigate this issue by capturing and aligning images from various angles, thereby enhancing resolution, particularly in the z-direction [25,26]. This underscores the necessity for imaging systems tailored to accommodate the algorithm, providing flexibility in sample orientation adjustments to achieve superior resolution and expand the scope of biological imaging [27]. Another limitation lies in the trade-off between resolution and field of view (FOV). Traditional LSFM techniques, utilizing a Gaussian beam to create the light sheet, benefit from a thin beam waist for higher axial resolution but suffer from a restricted FOV [28]. This becomes particularly problematic in applications requiring both high resolution and large FOV, such as large tissue sample imaging [28–31]. Therefore, there is a demand for innovative systems capable of combining a thin beam waist with an expansive FOV. Additionally, most LSFM systems expose the imaging media to air due to the practicality of loading and unloading samples [20,32], a setup that poses challenges when dealing with hazardous substances like dibenzyl ether (DBE). A system featuring a fully enclosed chamber would not only streamline the process but also enhance safety in LSFM imaging, marking a significant step forward in the field.

1.2 Tissue Clearing Techniques

To access structural and molecular information from intact tissues, optical clearing is essential. This process, designed to remove lipids, pigments, and calcium phosphate, matches the refractive indices (RIs) of the samples with the imaging media, achieving high transparency [33–36]. By effectively reducing light scattering and absorption, optical clearing enhances the microscope's capacity to investigate intact organs and thick tissues with exceptional precision and depth. [37] The field predominantly employs three types of methods: hydrophobic, hydrophilic, and hydrogel-based, with widely recognized protocols like iDISCO [38], CUBIC, and CLARITY [39], respectively [40–42].

In general, each type of clearing strategy possesses distinct strengths. Hydrophobic techniques are usually characterized by their speed [43]. They involve the use of organic solvents, which possess the ability to permanently preserve the samples, enabling multiple imaging sessions [44]. Hydrophilic methods usually lead to the formation of hydrogen bonds with molecules like proteins and surrounding water. This is beneficial for the preservation of the tissue structure and the fluorescence [45]. Hydrogel based approaches are particularly suitable for delicate samples as the hydrogel can minimize the damage to the structure of the samples [36].

1.3 LSFM with Tissue Clearing Methods

The integration of LSFM with tissue clearing techniques can take full advantage of both technologies. However, each optical clearing method corresponds to a different refractive index (RI) [46] , and typically, one method is best suited for a particular sample due to its unique features [36,47–51]. This poses a challenge, an LSFM system is typically designed for a specific RI by matching the sample, the tube, and the imaging media to that RI [52–56]. This specificity makes it challenging to explore all the clearing methods to find the most suitable one for a given sample because manufacturing chambers that match the different RIs of various imaging media is difficult. Additionally, while the RI of some imaging media can be fine-tuned within a range for optimal clearing performance [57], the RI of the chamber is not easily adjustable. Therefore, a system that can accommodate various imaging media with different refractive indices is highly desirable. Such a system would significantly facilitate the exploration of multiple clearing strategies across diverse sample types, greatly benefiting biological researchers.

1.4 Contributions of This Work

In this work, we propose a multi-channel multi-view LSFM system designed to allow synergetic adjustments of both the sample and the laser. Our rational design enables the system to 1) seamlessly accommodate varying refractive indices; 2) integrate multi-view reconstruction for enhanced isotropy and resolution; 3) axially sweep the beam waist and synchronize with the camera for an enlarged FOV without sacrificing resolution. Moreover, unlike LSFM systems that expose the imaging media [20,32], our system employs a secure and enclosed sample chamber. This design is particularly well-suited for handling hazardous and/or evaporating imaging media such as DBE. To demonstrate its capabilities, we imaged a variety of biological samples processed with different optical clearing methods, each matched to a specific refractive index. These samples included a mouse retina cleared by CLARITY (vasculature stained, RI=1.45), a mouse descending aorta cleared by iDISCO+ (neurons stained, RI=1.56), a mouse rainbow heart [58] cleared by CUBIC (cell progeny labeled, RI=1.52), and a *Tg(flk1:mcherry)* zebrafish in water (vasculature labeled, RI=1.33). The results from these diverse samples highlight the robustness and adaptability of our proposed system.

CHAPTER 2 Design of the Optical System

Our proposed system highlights the flexible positioning and rotation of the laser and sample chamber (Figure 2-1(a)). This feature allows for light sheet adjustment in synchrony to the chamber position to correct for focal shift induced by the imaging media refractive index mismatching. Additionally, it enables axial sweeping that maintains the thinnest beam waist in alignment with the camera's shutter, ensuring that the scanned line of pixels is always illuminated by the narrowest beam waist throughout entire field of view (Figure 2-1(b)). This setup stabilizes and maximizes image quality by minimizing scattering light. Furthermore, the free rotation capability allows for the use of multi-view reconstruction algorithm, which compensates for degraded axial resolution and provides isotropic spatial performance (Figure 2-1(c)). Light-sheet images also suffer from nonuniform illumination due to sample tissue scattering. The algorithm integrates multi-view measurements to optimize overall imaging quality.

Typically, the LSFM system is designed specifically for a particular RI (Figure 2-1(d)). The sample is immersed in a medium within a chamber holder, which is then placed into a large cuvette. To prevent light distortion, the RI of the sample, imaging medium, chamber, and immersion medium outside the chamber must be identical (Figure 2-1(e)). Any RI mismatch among these components causes light distortion due to refraction at the RI-mismatch interfaces (Figure 2-1(f-g)).

In our design, the sample is mounted directly into a small, closed cubic chamber (Figure 2-2(a)). While the detection objective remains fixed, the sample/chamber scans axially to generate a z-stack 3-D image. Due to the RI mismatch between the imaging media and the air, the chamber's movement shifts the focal plane, and the illuminated plane becomes defocused (Figure 2-1(h)). To address this, our system adjusts the light sheet position to compensate for the focal shift, ensuring that the illumination plane and the focal plane remain consistent (Figure 2-1(h)) The orthogonal design of the laser is calibrated within the optical system to achieve independent control of the translational shift of the laser in each direction (Figure 2-1(i), Figure 2-2(b)).

To access precise synchronization, the relationship between the chamber displacement ΔC, the laser displacement ΔL, and the sample displacement (the true z-step, ΔS) must be established as follows (Figure 2-1(i)):

$$C_2 - C_1 = \Delta C \qquad \text{(Eq. 1)}$$

$$L_2 - L_1 = \Delta L \qquad \text{(Eq. 2)}$$

$$\Delta S = -\Delta L + \Delta C \qquad \text{(Eq. 3)}$$

where C_1 and C_2 are the chamber positions before and after the shift, respectively, and L_1 and L_2 are the laser positions before and after the shift (Figure 2-1(i)).

From Snell's law:

$$R = \sin\theta_1 \,/\, \sin\theta_2 \qquad \text{(Eq. 4)}$$

where R is the RI of the imaging medium.

Given that we are imaging large tissues, and the detection objective has a low numerical aperture (NA) with a small objective aperture, the paraxial approximation can be applied to Eq. 4, simplifying it to:

$$R = \tan\theta_1 \,/\, \tan\theta_2 \qquad \text{(Eq. 5)}$$

Therefore:

$$R = (L_1 - C_1)/(F - C_1) \qquad \text{(Eq. 6)}$$

$$R = (L_2 - C_2)/(F - C_2) \qquad \text{(Eq. 7)}$$

where F is the virtual image of the focus point (Figure 2-1(i)).

Combining Eq. 1, Eq. 2, Eq. 3, Eq. 6 and Eq. 7:

$$\Delta S = \Delta C - \Delta L = \Delta C \cdot R \qquad \text{(Eq. 8)}$$

$$\Delta L = \Delta C(1 - R) \qquad \text{(Eq. 9)}$$

Eq. 8 and Eq. 9 demonstrate the relationship between ΔS, ΔL, and ΔC.

Figure 2-1(i) shows the schematic of the system. As indicated, there are two orthogonal designs within the system, allowing the laser to move independently in each direction.

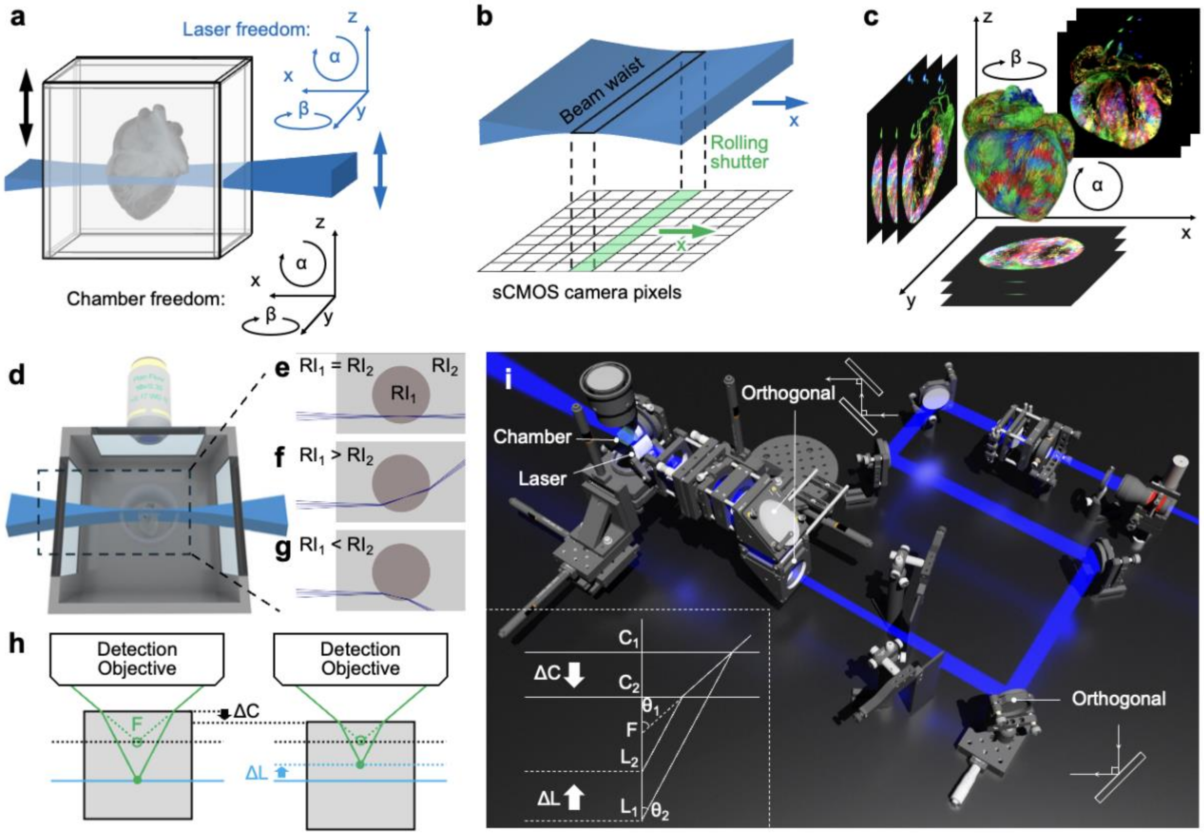

Figure 2-1. Schematic of the LSFM system. (a) The laser and chamber possess five degrees of translational and rotational freedom, enabling chamber-laser synchronization, axial sweeping, and multi-view reconstruction. (b) Axial sweeping design, where the thinnest beam waist is synchronized with the rolling shutter of the camera. (c) Multi-view reconstruction enhances isotropy and resolution. (d) A typical traditional LSFM system with the chamber placed in a large cuvette. (e-g) Scenarios depicting the components in d with refractive index (RI) matched or mismatched. (h) Illumination plane defocus when the chamber position shifts. Synchronously moving the laser compensates for the misalignment. (i) Schematic of the optical path and design of the LSFM system. Inset in (i): schematic used to derive the relationship between the laser, chamber, and sample.

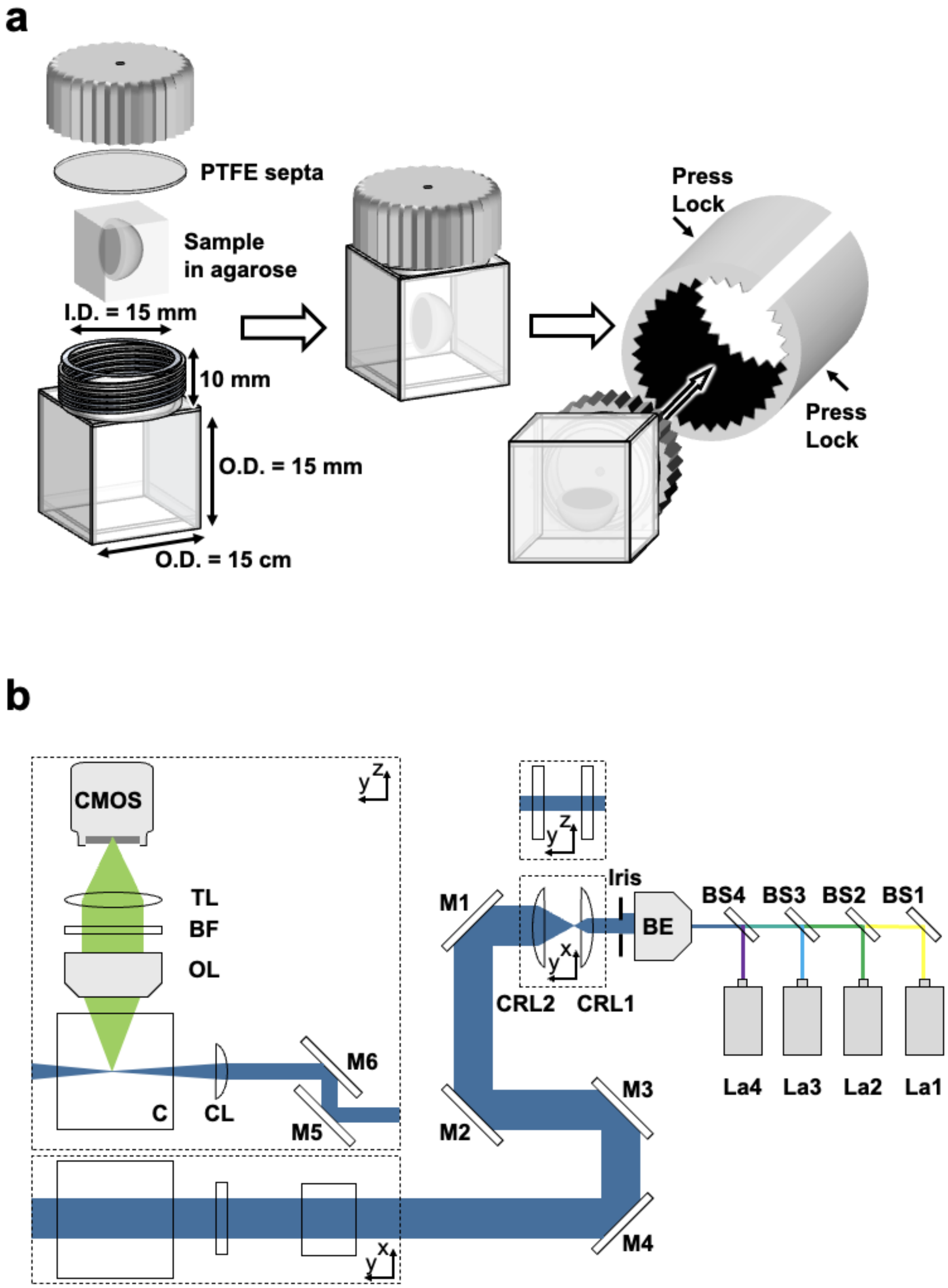

Figure 2-2. (a) Schematic of the sample chamber and the holder. (b) Optical path diagram of the LSFM system.

Even a slight difference in focal length can significantly degrade imaging quality, making the synchronization design a huge advantage. The point spread function (PSF) can be expressed as a function related to the RI, chamber position, and laser position. Therefore, synchronized adjustments of these two position variables can improve the PSF. As shown in Figure 2-3(a), with synchronization, PSF shows no difference when moving the chamber up to 5mm away from the original focal point. This stability is demonstrated by imaging in PBS and the mediums required in CLARITY and CUBIC. This indicates the imaging quality can be maintained at a high level throughout the imaging process. Without synchronization, however, PSF spread notably, meaning the clarity and the sharpness drop rapidly as the chamber moves. The synchronization design ensures that images are captured under the best configuration, thereby enhancing overall imaging accuracy.

The system does not only enhance imaging quality but also allows for the determination of unknown RI. Figure 2-3(b) shows the results of a blind PSF test using a medium with an RI of 1.52 in CUBIC-R+(M). Assuming this RI is unknow, we can hypothesize it to be 1.53 and start to image. We then subtly adjust the focal length to capture new images and conducting comparisons among various groups. Each time after comparison, we can know the direction to adjust focal distance (Figure 2-3(b)). The iterative process continues until the minimum PSF is identified, and subsequently the unknown RI can be confirmed.

Figure 2-3(c) demonstrates the image enhancement using multi-view algorithm. Due to the poor axial resolution of detection objective, each view shows elongated point spread function. It degrades the 3D images and hinders accurate quantification of sample structures. However, the views are complementary to each other, allowing for image enhancement by fusing them together. The multi-view algorithm first registers measurement from different view angles by correcting sample drift and other misalignments. It then combines registered images to generate a high-quality 3D representation of the sample. The algorithm significantly enhances the originally compromised image and restores isotropic resolution, enabling detailed spatial visualization of the sample.

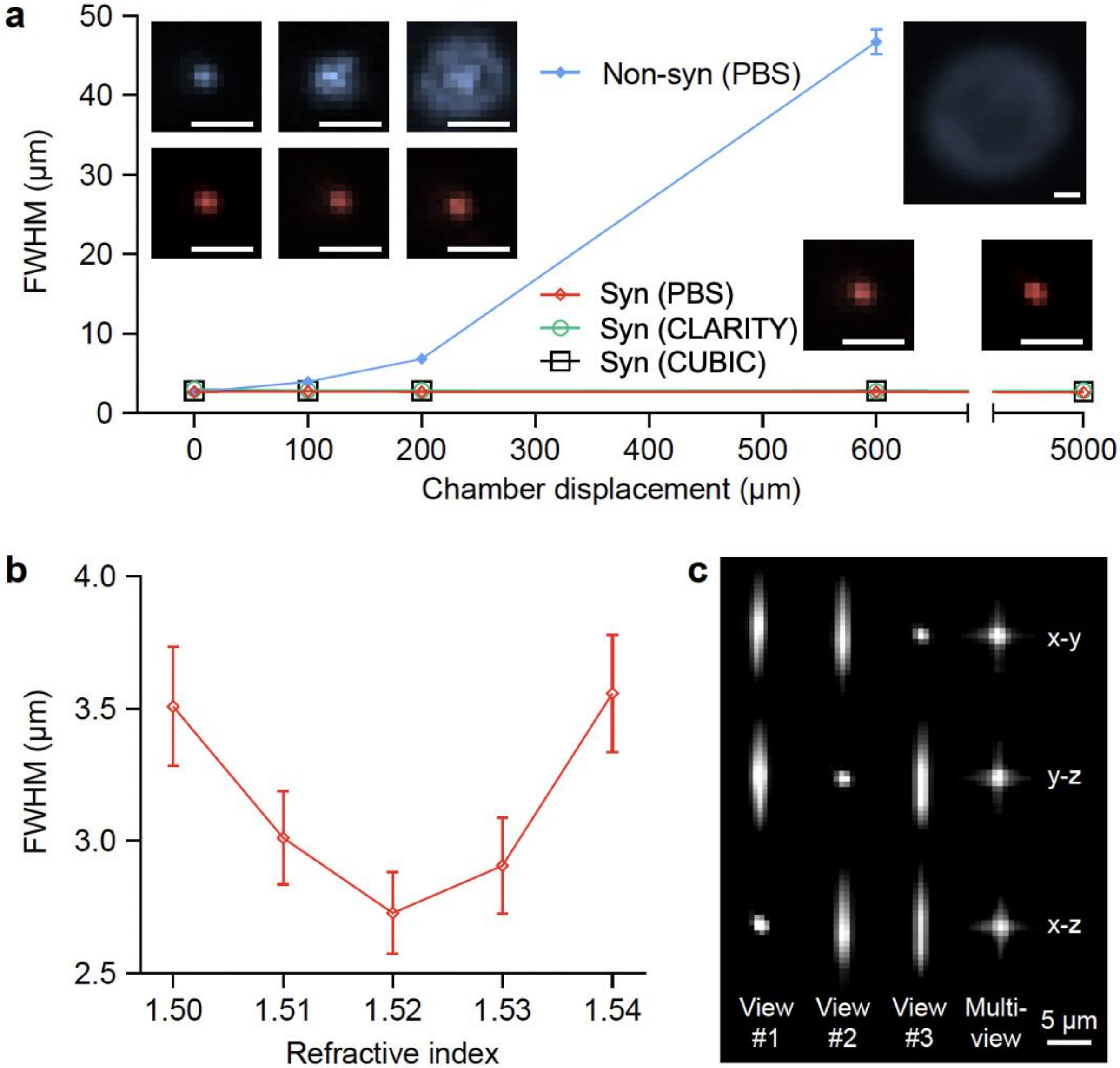

Figure 2-3. (a) Relationship between chamber displacement and PSF. The non-synchronized configuration leads to lower imaging quality, while the synchronized configuration maintains high-quality PSF under multiple sample processing conditions. (b) Measured PSF as a function of refractive index, with RI = 1.52. (c) Fluorescence bead images demonstrating the effect of the multi-view reconstruction algorithm.

CHAPTER 3 Imaging Results and Discussion

The need for a light-sheet system compatible with multiple RIs arises from the truth that common clearing methods require mediums with different RIs. For example, the RI of water is 1.33, while the RIs for the mediums used in CLARITY, CUBIC, and iDISCO+ are 1.46, 1.52, and 1.56, respectively (Figure 3-1(a), (b)). These clearing methods are all effective and widely used, each offering unique advantages that make them the optimal choice for specific research purposes. However, traditional light-sheet systems are usually designed for a fixed RI (Figure 2-1(d)). In this paper, we will demonstrate our light-sheet system's capability to work with various tissue clearing strategies by showing samples processed with different methods (Figure 3-1).

Live *Tg(flk1:mcherry)* zebrafish were imaged without clearing to study the development of endothelial cells within the vasculature. The zebrafish were placed in water for the imaging process (Figure 3-1(c)). Considering the fragility of retinas and the presence of delicate microvasculature, CALRITY was chosen to process the samples. CLARITY immerses the sample in gel rather than solutions, which helps preserve structural integrity. Endothelial cells were marked with Isolectin-B4 to promote the understanding of retinopathy (Figure 3-1(d)). For $\alpha\mathrm{MHC}^{\mathrm{Cre}}$; $\mathrm{R26}^{\mathrm{VT2/GK}}$ mouse hearts, which contain embryonic cardiomyocytes with endogenous fluorescence, CUBIC was used to clear the samples and preserve the fluorescent proteins, allowing for the imaging of cell progeny (Figure 3-1(e)). The relatively strong structure of the mouse aorta makes it suitable for quick immunolabeling. Therefore, iDISCO+ was chosen to process the descending aorta samples stained with anti-Tyrosine hydroxylase to study neurovascular interactions. For mouse descending aorta with marked tyrosine hydroxylase, 3D imaging is particularly necessary since the distribution of tyrosine hydroxylase is sparse and almost indistinguishable in 2D slices (Figure 3-1(f)).

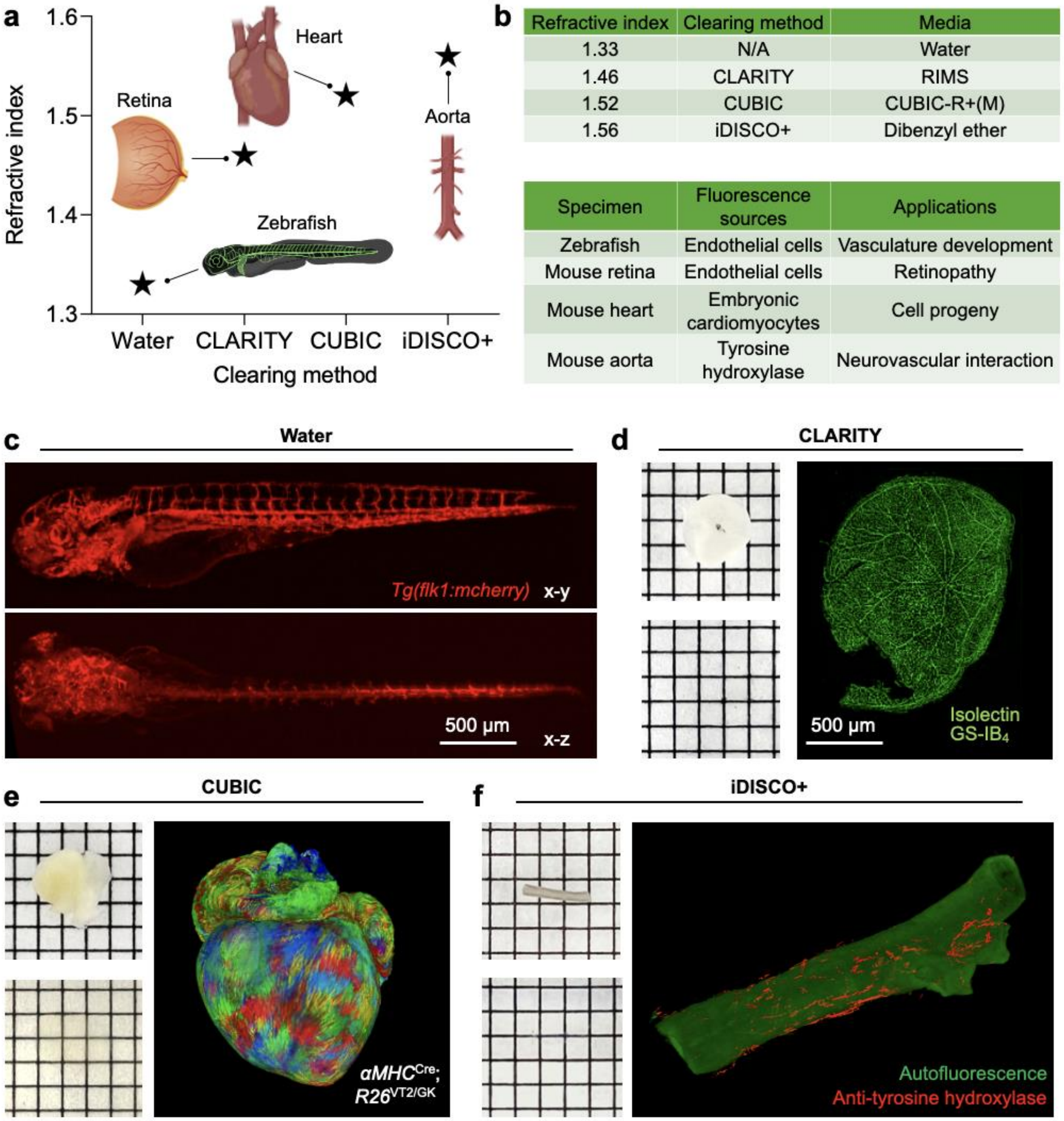

Refractive index	Clearing method	Media
1.33	N/A	Water
1.46	CLARITY	RIMS
1.52	CUBIC	CUBIC-R+(M)
1.56	iDISCO+	Dibenzyl ether

Specimen	Fluorescence sources	Applications
Zebrafish	Endothelial cells	Vasculature development
Mouse retina	Endothelial cells	Retinopathy
Mouse heart	Embryonic cardiomyocytes	Cell progeny
Mouse aorta	Tyrosine hydroxylase	Neurovascular interaction

Figure 3-1. (a) Samples are processed using different tissue clearing methods, each with media having various RIs. These samples have assorted fluorescence sources and support multiple applications. (b) x-y and x-z view of a *Tg (flk1: mcheery)* zebrafish in water, where endothelial cells express fluorescent proteins. (c) Mouse retina cleared with CLARITY. Vasculature endothelial cells are marked with Isolectin-B4. (d) αMHC^{Cre}; R26$^{VT2/GK}$ mouse heart cleared with CUBIC, displaying inherent green, blue, orange, and red fluorescence in clones. (e) Mouse descending aorta cleared with iDISCO+. Aorta is stained with anti-tyrosine hydroxylase antibody.

3. 1 Zebrafish in Water (RI=1.33)

The zebrafish model stands out as an ideal choice for light-sheet imaging due to its exceptional optical transparency. Within this model, the transgenic *Tg (flk1: mcherry)* zebrafish emerges as a valuable resource for investigating vasculature, as it effectively labels endothelial cells. This model empowers researchers to delve into structures associated with blood vessels, such as the blood-brain barrier, blood-retinal barrier [59], and the gut-vascular barrier [60]. Of particular significance, the gut-vascular barrier in this model offers a practical tool for studying the impact of environmental pollutants [21]. This barrier has been observed to be disrupted by ambient ultrafine particles, making it a suitable model for investigating the effects of environmental pollutants. Understanding how air pollution can lead to organ dysfunction is becoming increasingly critical, as pollution is recognized as one of the leading risk factors for mortality worldwide [61].

3.2 Mouse Retina Cleared by CLARITY (RI=1.45)

Anomalous retinal angiogenesis is a common factor in a multitude of eye diseases, including diabetic retinopathy (DR), glaucoma, age-related macular degeneration (AMD), and retinopathy of prematurity (ROP). Among these diseases, DR [62,63], glaucoma [64,65], and AMD [66] stand out as three of the primary culprits behind global blindness. While the specific pathways leading to vision loss may differ among these diseases, they all share a common hallmark: abnormal retinal vasculature structure [53,67–69]. Understanding and scrutinizing these abnormalities in retinal vasculature is paramount, as it provides valuable insights into the physiological processes at play and offers potential therapeutic avenues for treatment. As a result, the ability to effectively image vasculature in the mouse retina is an indispensable tool for unraveling the underlying pathologies and expediting advancements in the study of these sight-threatening eye diseases. Such imaging capabilities serve as a cornerstone for driving progress in the field of ophthalmology and ultimately hold the potential to improve the lives of countless individuals affected by these conditions.

Retina imaging showcased the advantage of axial sweeping and multi-view reconstruction algorithm. Figure 3-2(a) and (b) present the maximum intensity projections of mouse retina vasculature, with endothelial cells marked by Isolectin-B4. Figure 3-2(a1-a3) show zoom-in views of the left peripheral area, center area, and right peripheral area, respectively. The beam waist of the light sheet is scanned and synchronized with the camera rolling shutter. Consequently, it synthesizes a thin planar illumination across field of view without suffering from laser beam divergence. Our method provides sufficient resolution to distinctly visualize the vasculature. Figure 3-2(b) displays the vasculature imaged by light sheet without axial sweeping. In this configuration, the light sheet is focused on the left part of the sample, capturing only the line of pixels to the left of the retina under the thinnest beam waist. As scanning towards the right, the light beam thickens, resulting in progressively blurrier images. Figure 3-2 (b1-b3) correspond to the same positions in Figure 3-2(a). A similar comparison between single optical slices can be seen in Figure 3-2(c) and (d). With a uniform light beam, the three layers of the retina (Superficial layer vessels, intermediate layer vessels, and deep layer vessels) are clearly visible. However, as the light sheet's thickness expands due to the nature of gaussian beam, the imaging quality becomes worse. As a result, in Figure 3-2(d), although the left portion of the retina remains clear, the right portion appears significantly blurry, making it difficult to distinguish between the layers. Figure 3-2(e) presents three cross-sections of the retina. The first two images were captured without applying multi-view reconstruction algorithm. While the second image demonstrates good clarity, the first image appears to be blurry. After implementing multi-view reconstruction and re-slicing the sample, the third image shows a representative overall quality. As evident, the overall imaging quality has been significantly improved with minimal loss of clarity compared to the clearest view before the implementation. The above illustrations demonstrate the impact of light sheet divergence on imaging quality and underscore the importance of axial sweeping as well as multi-view reconstruction algorithm in maintaining superior image clarity. Additionally, these images indicate the system can maintain a large FOV without sacrificing resolution, as the diameter of mouse retinas reaches several millimeters.

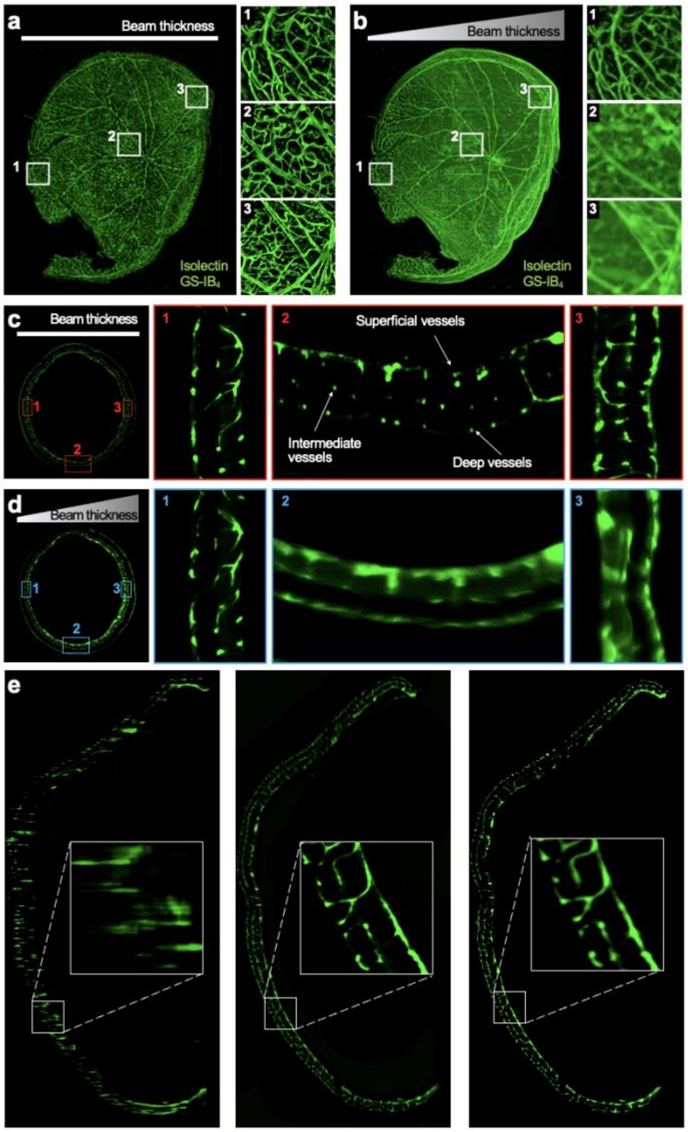

Figure 3-2. Imaging results of whole 2-month-old mouse retina vasculature. (a) Maximum intensity projection with consistent thinnest light beam. 1-3: Enlarged views of the left peripheral area, the center area, and the right peripheral area, respectively. (b) Maximum intensity projection with gradually increasing beam thickness. 1-3: Enlarged views of the same positions as in (a). (c) Optical slice with consistent thinnest light beam. 1-3: Enlarged views of representative areas from the left, bottom, and right parts. (d) Corresponding optical slice with gradually increasing beam thickness. 1-3: Enlarged views of the same areas as in (c). (e) Impact of multi-view reconstruction on z-slice quality. Left: a blurry cross-section from a sample imaged without multi-view reconstruction. Middle: the clearest cross-section from the same sample without multi-view reconstruction. Right: a representative cross-section after multi-view reconstruction.

3.3 αMHC^{Cre}; R26$^{VT2/GK}$ Mouse Rainbow Heart Cleared by CUBIC, (RI=1.52)

The mechanisms underlying the formation of cardiac tissue remain a realm of mystery, primarily due to the remarkable complexity of both the structure and function of the heart. In this intricate landscape, the rainbow system emerges as an innovative tool, offering the ability to mark a limited number of cells and their descendant cells with unique fluorescent proteins in a stochastic manner. This enables retrospective tracing of cellular expansion through distinct, identifiable clones [70]. When applied to the mouse heart, the rainbow system becomes an invaluable asset for researchers. It allows for the identification of the sources of newly generated cells during heart development and in response to injury. This, in turn, facilitates investigations into the proliferative potential of cardiac cells, including cardiomyocytes [58], at different stages of life, ranging from embryonic development to adulthood. By shedding light on the origins and dynamics of cardiac cell growth, the rainbow system holds the promise of unlocking new insights into the formation and regenerative capacity of cardiac tissue, ultimately advancing our understanding of cardiac biology.

In this study, αMHC^{Cre}; R26$^{VT2/GK}$ mice were used to observe the proliferative activity of cardiomyocytes. The αMHC promoter is primarily expressed in cardiomyocytes, enabling the induction of the Cre system in mouse hearts. Thus, the cross of αMHC^{Cre} and R26$^{VT2/GK}$ may randomly lead to four potential gene deletion situations (Figure 3-3(a)) These deletions inherently mark embryonic cardiomyocytes in clones with green, blue, orange, and red fluorescence colors. These colors are passed on to subsequent cell generations during differentiation, aiding researchers in tracking proliferation. Figure 3-3(b) shows the reconstructed E18.5 αMHC^{Cre}; R26$^{VT2/GK}$ mouse heart. The distribution of various colors can be seen clearly. As shown in Figure 3-3(c-e), different heart structures are distinguishable. Traditionally, similar research is conducted by sample sectioning and confocal imaging. However, compared to these methods, the optical sections of 3D light-sheet imaging not only demonstrate satisfactory resolution but also preserve structural information more effectively, as physical sample sectioning often results in deformation. Altogether, the combination of $\alpha\text{MHC}^{\text{Cre}}$; $\text{R26}^{\text{VT2/GK}}$ mouse hearts with this light-sheet system enables clear visualization of the progeny of different cell types, supporting the study of cell differentiation in the mouse heart.

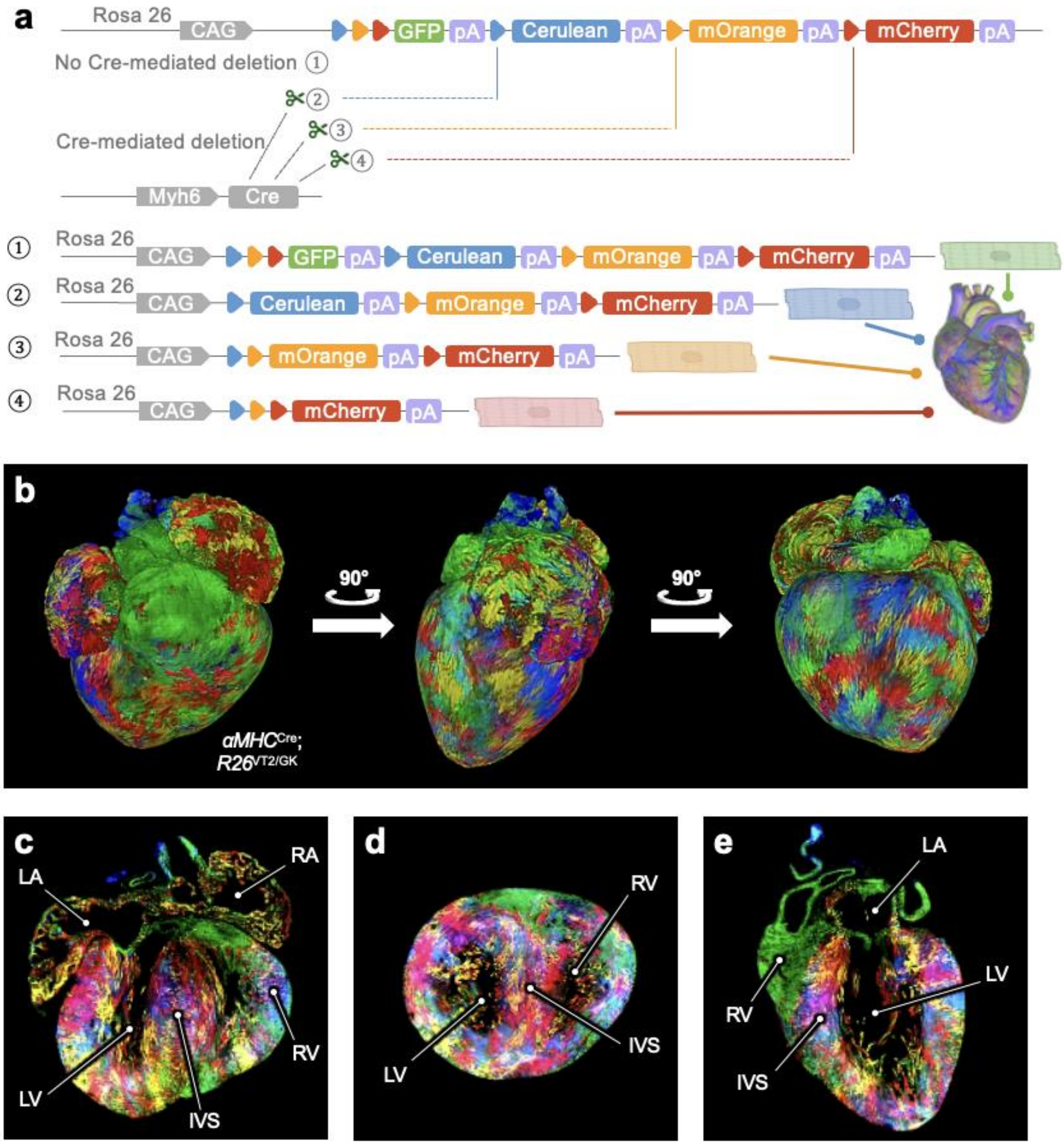

Figure 3-3. (a) Illustration of four Cre-induced deletion scenarios. Each deletion leads to one distinct clone color (① - green, ② - blue, ③ - orange, ④ - red). (b) Schematic of multi-view imaging. The sample is rotated 90 degree each time before the set of images is taken. (c-e) Representative images of the mouse rainbow heart.

CHAPTER 4 Conclusion

In this work, we have presented a light-sheet system capable of adapting to flexible RI, enabling exploration of various tissue clearing methods across diverse biological samples. The features of the system are evaluated by its PSF. *Tg(flk1:mcherry)* zebrafish in water, mouse retina cleared by CLARITY, αMHC^{Cre}; $R26^{VT2/GK}$ mouse rainbow heart cleared by CUBIC, and mouse descending aorta cleared by iDISCO+ were chosen to represent scenarios when RI equals 1.33, 1.45, 1.52 and 1.56, respectively. Through the utilization of above biological samples with differing tissues, sizes, and processing approaches, we have demonstrated the significance of combining axial sweeping and multi-view reconstruction. By incorporating these features, our system effectively corrects defocus caused by RI mismatching, identifies the RI of unknown mediums, ensures comprehensive tissue clearing compatibility, and delivers isotropic high-resolution images across large FOV. We believe that our system greatly expands the range of applications accessible to a single optical system. Furthermore, it holds promise for benefiting other biological researchers and inspiring within the light community to develop novel configurations for similar research and applications.

References

1. K. Thorn, "A quick guide to light microscopy in cell biology," MBoC **27**, 219–222 (2016).
2. A. D. Elliott, "Confocal Microscopy: Principles and Modern Practices," Curr Protoc Cytom **92**, e68 (2020).
3. W. Denk, J. H. Strickler, and W. W. Webb, "Two-Photon Laser Scanning Fluorescence Microscopy," Science **248**, 73–76 (1990).
4. J. Shaya, P. Corridon, B. Al-Omari, A. Mh, A. Shunnar, M. Infas, A. Qurashi, B. Michel, and A. Burger, "Design, Photophysical Properties, and Applications of Fluorene-Based Fluorophores in Two-Photon Fluorescence Bioimaging: a Review," Journal of Photochemistry and Photobiology C: Photochemistry Reviews **52**, 100529 (2022).
5. K. K. McKayed and J. C. Simpson, "Actin in Action: Imaging Approaches to Study Cytoskeleton Structure and Function," Cells **2**, 715–731 (2013).
6. S.-L. Liu, Z.-G. Wang, H.-Y. Xie, A.-A. Liu, D. C. Lamb, and D.-W. Pang, "Single-Virus Tracking: From Imaging Methodologies to Virological Applications," Chem. Rev. **120**, 1936–1979 (2020).
7. S. Li, R. Chang, L. Zhao, R. Xing, J. C. M. van Hest, and X. Yan, "Two-photon nanoprobes based on bioorganic nanoarchitectonics with a photo-oxidation enhanced emission mechanism," Nat Commun **14**, 5227 (2023).
8. G. C. R. Ellis-Davies, "Two-Photon Microscopy for Chemical Neuroscience," ACS Chem Neurosci **2**, 185–197 (2011).
9. J. Jonkman, C. M. Brown, G. D. Wright, K. I. Anderson, and A. J. North, "Tutorial: guidance for quantitative confocal microscopy," Nat Protoc **15**, 1585–1611 (2020).

10. F. Helmchen and W. Denk, "Deep tissue two-photon microscopy," Nat Methods **2**, 932–940 (2005).

11. R. K. P. Benninger and D. W. Piston, "Two-photon excitation microscopy for the study of living cells and tissues," Curr Protoc Cell Biol **Chapter 4**, 4.11.1-4.11.24 (2013).

12. K. Svoboda and R. Yasuda, "Principles of two-photon excitation microscopy and its applications to neuroscience," Neuron **50**, 823–839 (2006).

13. J. Huisken, J. Swoger, F. Del Bene, J. Wittbrodt, and E. H. K. Stelzer, "Optical Sectioning Deep Inside Live Embryos by Selective Plane Illumination Microscopy," Science **305**, 1007–1009 (2004).

14. B.-C. Chen, W. R. Legant, K. Wang, L. Shao, D. E. Milkie, M. W. Davidson, C. Janetopoulos, X. S. Wu, J. A. Hammer, Z. Liu, B. P. English, Y. Mimori-Kiyosue, D. P. Romero, A. T. Ritter, J. Lippincott-Schwartz, L. Fritz-Laylin, R. D. Mullins, D. M. Mitchell, J. N. Bembenek, A.-C. Reymann, R. Böhme, S. W. Grill, J. T. Wang, G. Seydoux, U. S. Tulu, D. P. Kiehart, and E. Betzig, "Lattice light-sheet microscopy: Imaging molecules to embryos at high spatiotemporal resolution," Science **346**, 1257998 (2014).

15. J. Schöneberg, D. Dambournet, T.-L. Liu, R. Forster, D. Hockemeyer, E. Betzig, and D. G. Drubin, "4D cell biology: big data image analytics and lattice light-sheet imaging reveal dynamics of clathrin-mediated endocytosis in stem cell–derived intestinal organoids," MBoC **29**, 2959–2968 (2018).

16. O. E. Olarte, J. Andilla, E. J. Gualda, and P. Loza-Alvarez, "Light-sheet microscopy: a tutorial," Adv. Opt. Photon., AOP **10**, 111–179 (2018).

17. K. M. Dean, T. Chakraborty, S. Daetwyler, G. Garrelts, O. M'Saad, H. T. Mekbib, F. F. Voigt, M. Schaettin, E. T. Stoeckli, F. Helmchen, J. Bewersdorf, and R. Fiolka, "Isotropic

Imaging Across Spatial Scales with Axially Swept Light-Sheet Microscopy," Nat Protoc **17**, 2025–2053 (2022).

18. A. K. Pediredla, S. Zhang, B. Avants, F. Ye, S. Nagayama, Z. Chen, C. Kemere, J. T. Robinson, and A. Veeraraghavan, "Deep imaging in scattering media with selective plane illumination microscopy," JBO **21**, 126009 (2016).
19. Z. Wang, Y. Ding, S. Satta, M. Roustaei, P. Fei, and T. K. Hsiai, "A hybrid of light-field and light-sheet imaging to study myocardial function and intracardiac blood flow during zebrafish development," PLOS Computational Biology **17**, e1009175 (2021).
20. Y. Ding, J. Ma, A. D. Langenbacher, K. I. Baek, J. Lee, C.-C. Chang, J. J. Hsu, R. P. Kulkarni, J. Belperio, W. Shi, S. Ranjbarvaziri, R. Ardehali, Y. Tintut, L. L. Demer, J.-N. Chen, P. Fei, R. R. S. Packard, and T. K. Hsiai, "Multiscale light-sheet for rapid imaging of cardiopulmonary system," JCI Insight **3**, (2018).
21. S. Gonzalez-Ramos, J. Wang, J. M. Cho, E. Zhu, S.-K. Park, J. G. In, S. T. Reddy, E. F. Castillo, M. J. Campen, and T. K. Hsiai, "Integrating 4-D light-sheet fluorescence microscopy and genetic zebrafish system to investigate ambient pollutants-mediated toxicity," Science of The Total Environment **902**, 165947 (2023).
22. H. Kafian, M. Lalenejad, S. Moradi-Mehr, S. A. Birgani, and D. Abdollahpour, "Light-Sheet Fluorescence Microscopy with Scanning Non-diffracting Beams," Sci Rep **10**, 8501 (2020).
23. Y. Gan, Y. Ma, W. Gong, W. Liu, Z. Wang, X. Hao, Y. Han, C. Kuang, and X. Liu, "Enhanced axial resolution of lattice light sheet microscopy by fluorescence differential detection," Opt Express **30**, 27381–27394 (2022).

24. E. H. K. Stelzer, F. Strobl, B.-J. Chang, F. Preusser, S. Preibisch, K. McDole, and R. Fiolka, "Light sheet fluorescence microscopy," Nat Rev Methods Primers **1**, 1–25 (2021).

25. S. Preibisch, S. Saalfeld, J. Schindelin, and P. Tomancak, "Software for bead-based registration of selective plane illumination microscopy data," Nat Methods **7**, 418–419 (2010).

26. S. Preibisch, F. Amat, E. Stamataki, M. Sarov, R. H. Singer, E. Myers, and P. Tomancak, "Efficient Bayesian-based multiview deconvolution," Nat Methods **11**, 645–648 (2014).

27. Y. Wu, X. Han, Y. Su, M. Glidewell, J. S. Daniels, J. Liu, T. Sengupta, I. Rey-Suarez, R. Fischer, A. Patel, C. Combs, J. Sun, X. Wu, R. Christensen, C. Smith, L. Bao, Y. Sun, L. H. Duncan, J. Chen, Y. Pommier, Y.-B. Shi, E. Murphy, S. Roy, A. Upadhyaya, D. Colón-Ramos, P. La Riviere, and H. Shroff, "Multiview confocal super-resolution microscopy," Nature **600**, 279–284 (2021).

28. C. Liu, C. Bai, X. Yu, S. Yan, Y. Zhou, X. Li, J. Min, Y. Yang, D. Dan, and B. Yao, "Extended field of view of light-sheet fluorescence microscopy by scanning multiple focus-shifted Gaussian beam arrays," Opt. Express, OE **29**, 6158–6168 (2021).

29. T. Vettenburg, H. I. C. Dalgarno, J. Nylk, C. Coll-Lladó, D. E. K. Ferrier, T. Čižmár, F. J. Gunn-Moore, and K. Dholakia, "Light-sheet microscopy using an Airy beam," Nat Methods **11**, 541–544 (2014).

30. C. Akitegetse, T. Charland, M. Quémener, C. Gora, V. Rioux, M. Piché, Y. De Koninck, M. Lévesque, and D. C. Côté, "Millimetric scale two-photon Bessel-Gauss beam light sheet microscopy with three-axis isotropic resolution using an axicon lens," Neurophotonics **10**, 035002 (2023).

31. B. Xiong, X. Han, J. Wu, H. Xie, and Q. Dai, "Improving axial resolution of Bessel beam light-sheet fluorescence microscopy by photobleaching imprinting," Opt. Express, OE **28**, 9464–9476 (2020).
32. S. L. Logan, C. Dudley, R. P. Baker, M. J. Taormina, E. A. Hay, and R. Parthasarathy, "Automated high-throughput light-sheet fluorescence microscopy of larval zebrafish," PLOS ONE **13**, e0198705 (2018).
33. M. Pende, K. Vadiwala, H. Schmidbaur, A. W. Stockinger, P. Murawala, S. Saghafi, M. P. S. Dekens, K. Becker, R. Revilla-I-Domingo, S.-C. Papadopoulos, M. Zurl, P. Pasierbek, O. Simakov, E. M. Tanaka, F. Raible, and H.-U. Dodt, "A versatile depigmentation, clearing, and labeling method for exploring nervous system diversity," Sci Adv **6**, eaba0365 (2020).
34. T. Yu, J. Zhu, D. Li, and D. Zhu, "Physical and chemical mechanisms of tissue optical clearing," iScience **24**, 102178 (2021).
35. H. Mesa, J. Meade, P. Gajewski-Kurdziel, R. D. Blakely, and Q. Zhang, "Simple Rescue of Opaque Tissue Previously Cleared by iDISCO," Bio Protoc **14**, e4948 (2024).
36. H. R. Ueda, A. Ertürk, K. Chung, V. Gradinaru, A. Chédotal, P. Tomancak, and P. J. Keller, "Tissue clearing and its applications in neuroscience," Nat Rev Neurosci **21**, 61–79 (2020).
37. T. Tian, Z. Yang, and X. Li, "Tissue clearing technique: Recent progress and biomedical applications," Journal of Anatomy **238**, 489–507 (2021).
38. V. Nudell, Y. Wang, Z. Pang, N. K. Lal, M. Huang, N. Shaabani, W. Kanim, J. Teijaro, A. Maximov, and L. Ye, "HYBRiD: hydrogel-reinforced DISCO for clearing mammalian bodies," Nat Methods **19**, 479–485 (2022).
39. H. Du, P. Hou, W. Zhang, and Q. Li, "Advances in CLARITY-based tissue clearing and imaging," Exp Ther Med **16**, 1567–1576 (2018).

40. R. Tomer, L. Ye, B. Hsueh, and K. Deisseroth, "Advanced CLARITY for rapid and high-resolution imaging of intact tissues," Nat Protoc **9**, 1682–1697 (2014).

41. R. Tomer and K. Deisseroth, "Rapid High-resolution Brain Mapping with CLARITY Optimized Light Sheet Microscopy (COLM)," Microsc Microanal **21**, 717–718 (2015).

42. C. Hahn, K. Becker, S. Saghafi, M. Pende, A. Avdibašić, M. Foroughipour, D. E. Heinz, C. T. Wotjak, and H.-U. Dodt, "High-resolution imaging of fluorescent whole mouse brains using stabilised organic media (sDISCO)," J Biophotonics **12**, e201800368 (2019).

43. A. Klingberg, A. Hasenberg, I. Ludwig-Portugall, A. Medyukhina, L. Männ, A. Brenzel, D. R. Engel, M. T. Figge, C. Kurts, and M. Gunzer, "Fully Automated Evaluation of Total Glomerular Number and Capillary Tuft Size in Nephritic Kidneys Using Lightsheet Microscopy," J Am Soc Nephrol **28**, 452–459 (2017).

44. F. Casoni, S. A. Malone, M. Belle, F. Luzzati, F. Collier, C. Allet, E. Hrabovszky, S. Rasika, V. Prevot, A. Chédotal, and P. Giacobini, "Development of the neurons controlling fertility in humans: new insights from 3D imaging and transparent fetal brains," Development **143**, 3969–3981 (2016).

45. Q.-H. Shan, X.-Y. Qin, N. Zhou, C. Huang, Y. Wang, P. Chen, and J.-N. Zhou, "A method for ultrafast tissue clearing that preserves fluorescence for multimodal and longitudinal brain imaging," BMC Biology **20**, 77 (2022).

46. F. F. Voigt, A. M. Reuss, T. Naert, S. Hildebrand, M. Schaettin, A. L. Hotz, L. Whitehead, A. Bahl, S. C. F. Neuhauss, A. Roebroeck, E. T. Stoeckli, S. S. Lienkamp, A. Aguzzi, and F. Helmchen, "Reflective multi-immersion microscope objectives inspired by the Schmidt telescope," Nat Biotechnol 1–7 (2023).

47. A. Greenbaum, K. Y. Chan, T. Dobreva, D. Brown, D. H. Balani, R. Boyce, H. M. Kronenberg, H. J. McBride, and V. Gradinaru, "Bone CLARITY: Clearing, imaging, and computational analysis of osteoprogenitors within intact bone marrow," Science Translational Medicine **9**, eaah6518 (2017).

48. E. A. Susaki, K. Tainaka, D. Perrin, F. Kishino, T. Tawara, T. M. Watanabe, C. Yokoyama, H. Onoe, M. Eguchi, S. Yamaguchi, T. Abe, H. Kiyonari, Y. Shimizu, A. Miyawaki, H. Yokota, and H. R. Ueda, "Whole-Brain Imaging with Single-Cell Resolution Using Chemical Cocktails and Computational Analysis," Cell **157**, 726–739 (2014).

49. K. Tainaka, T. C. Murakami, E. A. Susaki, C. Shimizu, R. Saito, K. Takahashi, A. Hayashi-Takagi, H. Sekiya, Y. Arima, S. Nojima, M. Ikemura, T. Ushiku, Y. Shimizu, M. Murakami, K. F. Tanaka, M. Iino, H. Kasai, T. Sasaoka, K. Kobayashi, K. Miyazono, E. Morii, T. Isa, M. Fukayama, A. Kakita, and H. R. Ueda, "Chemical Landscape for Tissue Clearing Based on Hydrophilic Reagents," Cell Rep **24**, 2196-2210.e9 (2018).

50. B. Yang, J. B. Treweek, R. P. Kulkarni, B. E. Deverman, C.-K. Chen, E. Lubeck, S. Shah, L. Cai, and V. Gradinaru, "Single-cell phenotyping within transparent intact tissue through whole-body clearing," Cell **158**, 945–958 (2014).

51. V. Gradinaru, J. Treweek, K. Overton, and K. Deisseroth, "Hydrogel-Tissue Chemistry: Principles and Applications," Annual Review of Biophysics **47**, 355–376 (2018).

52. J. Lee, P. Fei, R. R. S. Packard, H. Kang, H. Xu, K. I. Baek, N. Jen, J. Chen, H. Yen, C.-C. J. Kuo, N. C. Chi, C.-M. Ho, R. Li, and T. K. Hsiai, "4-Dimensional light-sheet microscopy to elucidate shear stress modulation of cardiac trabeculation," J Clin Invest **126**, 1679–1690 (2016).

53. C.-C. Chang, A. Chu, S. Meyer, Y. Ding, M. M. Sun, P. Abiri, K. I. Baek, V. Gudapati, X. Ding, P. Guihard, K. I. Bostrom, S. Li, L. K. Gordon, J. J. Zheng, and T. K. Hsiai, "Three-dimensional Imaging Coupled with Topological Quantification Uncovers Retinal Vascular Plexuses Undergoing Obliteration," Theranostics **11**, 1162–1175 (2021).

54. Y. Ding, A. Abiri, P. Abiri, S. Li, C.-C. Chang, K. I. Baek, J. J. Hsu, E. Sideris, Y. Li, J. Lee, T. Segura, T. P. Nguyen, A. Bui, R. R. S. Packard, P. Fei, and T. K. Hsiai, "Integrating light-sheet imaging with virtual reality to recapitulate developmental cardiac mechanics," JCI Insight **2**, (2017).

55. Z. Wang, L. Zhu, H. Zhang, G. Li, C. Yi, Y. Li, Y. Yang, Y. Ding, M. Zhen, S. Gao, T. K. Hsiai, and P. Fei, "Real-time volumetric reconstruction of biological dynamics with light-field microscopy and deep learning," Nat Methods **18**, 551–556 (2021).

56. P. Fei, J. Nie, J. Lee, Y. Ding, S. Li, H. Zhang, M. Hagiwara, T. Yu, T. Segura, C.-M. Ho, D. Zhu, and T. K. Hsiai, "Subvoxel light-sheet microscopy for high-resolution high-throughput volumetric imaging of large biomedical specimens," Advanced Photonics **1**, 016002 (2019).

57. T. Boothe, L. Hilbert, M. Heide, L. Berninger, W. B. Huttner, V. Zaburdaev, N. L. Vastenhouw, E. W. Myers, D. N. Drechsel, and J. C. Rink, "A tunable refractive index matching medium for live imaging cells, tissues and model organisms," eLife **6**, e27240 (2017).

58. K.-I. Sereti, N. B. Nguyen, P. Kamran, P. Zhao, S. Ranjbarvaziri, S. Park, S. Sabri, J. L. Engel, K. Sung, R. P. Kulkarni, Y. Ding, T. K. Hsiai, K. Plath, J. Ernst, D. Sahoo, H. K. A. Mikkola, M. L. Iruela-Arispe, and R. Ardehali, "Analysis of cardiomyocyte clonal expansion during mouse heart development and injury," Nat Commun **9**, 754 (2018).

59. J. Xie, E. Farage, M. Sugimoto, and B. Anand-Apte, "A novel transgenic zebrafish model for blood-brain and blood-retinal barrier development," BMC Dev Biol **10**, 76 (2010).
60. K. I. Baek, Y. Qian, C.-C. Chang, R. O’Donnell, E. Soleimanian, C. Sioutas, R. Li, and T. K. Hsiai, "An Embryonic Zebrafish Model to Screen Disruption of Gut-Vascular Barrier upon Exposure to Ambient Ultrafine Particles," Toxics **8**, 107 (2020).
61. R. Fuller, P. J. Landrigan, K. Balakrishnan, G. Bathan, S. Bose-O’Reilly, M. Brauer, J. Caravanos, T. Chiles, A. Cohen, L. Corra, M. Cropper, G. Ferraro, J. Hanna, D. Hanrahan, H. Hu, D. Hunter, G. Janata, R. Kupka, B. Lanphear, M. Lichtveld, K. Martin, A. Mustapha, E. Sanchez-Triana, K. Sandilya, L. Schaefli, J. Shaw, J. Seddon, W. Suk, M. M. Téllez-Rojo, and C. Yan, "Pollution and health: a progress update," Lancet Planet Health **6**, e535–e547 (2022).
62. N. Cheung, P. Mitchell, and T. Y. Wong, "Diabetic retinopathy," Lancet **376**, 124–136 (2010).
63. S. Sivaprasad, B. Gupta, R. Crosby-Nwaobi, and J. Evans, "Prevalence of diabetic retinopathy in various ethnic groups: a worldwide perspective," Surv Ophthalmol **57**, 347–370 (2012).
64. R. George, S. Panda, and L. Vijaya, "Blindness in glaucoma: primary open-angle glaucoma versus primary angle-closure glaucoma—a meta-analysis," Eye **36**, 2099–2105 (2022).
65. S. S.-Y. Lee and D. A. Mackey, "Glaucoma - risk factors and current challenges in the diagnosis of a leading cause of visual impairment," Maturitas **163**, 15–22 (2022).
66. J. W. Miller, L. L. D’Anieri, D. Husain, J. B. Miller, and D. G. Vavvas, "Age-Related Macular Degeneration (AMD): A View to the Future," Journal of Clinical Medicine **10**, 1124 (2021).

67. T. R. P. Taylor, M. J. Menten, D. Rueckert, S. Sivaprasad, and A. J. Lotery, "The role of the retinal vasculature in age-related macular degeneration: a spotlight on OCTA," Eye (Lond) **38**, 442–449 (2024).

68. X. Wang, M. Wang, H. Liu, K. Mercieca, J. Prinz, Y. Feng, and V. Prokosch, "The Association between Vascular Abnormalities and Glaucoma-What Comes First?," Int J Mol Sci **24**, 13211 (2023).

69. Z. Sun, D. Yang, Z. Tang, D. S. Ng, and C. Y. Cheung, "Optical coherence tomography angiography in diabetic retinopathy: an updated review," Eye (Lond) **35**, 149–161 (2021).

70. K. Kolluri, T. Nazarian, and R. Ardehali, "Clonal Tracing of Heart Regeneration," J Cardiovasc Dev Dis **9**, 141 (2022).